Nano Research
2023, 16(5): 6903

ISSN 1998-0124 CN 11-5974/O4
https://doi.org/10.1007/s12274-023-5445-0

Research Article

Metal oxyacid salts-confined pyrolysis towards hierarchical porous metal oxide@carbon (MO@C) composites as lithium-ion battery anodes

Huizhong Xu[1], Chang Gao[1], Zhaoyang Cheng[1], Linghui Kong[1], Wei Li[2] (✉), Xiaochen Dong[3], and Jianjian Lin[1] (✉)

[1] *Key Laboratory of Optic-electric Sensing and Analytical Chemistry for Life Science, Ministry of Education (MOE), Shandong Key Laboratory of Biochemical Analysis, College of Chemistry and Molecular Engineering, Qingdao University of Science and Technology, Qingdao 266042, China*
[2] *Engineering Research Center of High Performance Polymer and Molding Technology, Ministry of Education, Qingdao University of Science and Technology, Qingdao 266042, China*
[3] *Key Laboratory of Flexible Electronics (KLOFE) & Institute of Advanced Materials (IAM), Nanjing Tech University (NanjingTech), Nanjing, 211800, China*

Received: 25 October 2022 / **Revised:** 9 December 2022 / **Accepted:** 25 December 2022

ABSTRACT

Transition metal oxides (TMOs) have been thought of potential anodic materials for lithium-ion batteries (LIBs) owing to their intriguing properties. However, the limited conductivity and drastic volume change still hinder their practical applications. Herein, a metal oxyacid salts-confined pyrolysis strategy is proposed to construct hierarchical porous metal oxide@carbon (MO@C, MO = MoO_2, V_2O_5, and WO_3) composites for solving the aforementioned problems. A water-evaporation-induced self-assembly mechanism has been put forward for fabricating the MO@polyvinyl pyrrolidone (PVP)@SiO_2 precursors. After the following pyrolysis and etching process, small MO nanoparticles can be successfully encapsulated in the hierarchical porous carbon framework. Profiting from the synergistic effect of MO nanoparticles and highly conductive carbon framework, MO@C composites show excellent electrochemical properties. For example, the as-obtained MoO_2@C composite exhibits a large discharge capacity (1513.7 mAh·g^{-1} at 0.1 A·g^{-1}), good rate ability (443.5 mAh·g^{-1} at 5.0 A·g^{-1}), and supernal long-lived stability (669.1 mAh·g^{-1} after 1000 cycles at 1.0 A·g^{-1}). This work will inspire the design of novel anode materials for high-performance LIBs.

KEYWORDS

transition metal oxides, hierarchical porous carbon framework, anode materials, lithium storage performance

1 Introduction

The concurrent issues of energy crisis and environmental pollution have made the transform of worldwide energy structure from traditional fossil fuels to renewable energy resources become an inevitable trend [1, 2]. However, pertinent problems like intermittency and instability nature exist in the usage process of renewable energies, which largely limits their widespread applications. To this end, unremitting efforts are made on developing large-scale energy storage systems (EESs) to store the electric energy produced by these renewable sources, integrate them into electricity grids and deliver to thousands of families [3]. Among all sorts of EESs, lithium-ion batteries (LIBs) are the utmost used in everyday life, which have achieved remarkable success in various fields, ranging from tiny consumer electronics like cellular phones to large electric vehicles [4–6]. Nonetheless, in the advocacy of low-carbon life and the prevalence of new energy automobiles today, the requirements of high-performance LIBs are still increasingly stringent. Accordingly, substantial efforts are necessitated to further improve the electrochemical properties of LIBs.

As we know, among all the components of a battery, electrode materials where the electrochemical reaction takes place, are the critical part to break through the boundaries that beset commercial LIBs [7, 8]. In this regard, great efforts are focused on exploiting advanced electrode materials with high capacity, good rate capability, and cycling longevity [9]. Recently, transition metal oxides (TMOs), as appealing candidate of anode materials, have been extensively studied because of their intriguing properties, such as high theoretical capacity, environmental benignity, cost effectiveness, and intrinsic safety (vs. Li^+/Li) [10–12]. Most of TMOs, like cobalt oxide (Co_3O_4), ferric oxide (Fe_2O_3), and molybdenum dioxide (MoO_2), are subordinate to conversion-type anode materials, and thus have high theoretical specific capacities. While the other part of TMOs, such as titanium dioxide (TiO_2) and vanadium pentoxide (V_2O_5), are storing lithium through reversible intercalation and extraction reactions, and have relatively low theoretical specific capacities [13]. In addition, compared with graphite, TMOs have a higher working potential (about 1.0–1.3 V vs. Li^+/Li), which is benefit for the safety and stability of LIBs [13]. As the above advantages, TMOs are in the envious position of being a substitute of commercial graphite anode. Unfortunately, some intractable issues are still plaguing

Address correspondence to Wei Li, weilipku@hotmail.com; Jianjian Lin, Jianjian_Lin@qust.edu.cn

清華大學出版社 Tsinghua University Press Springer

TMOs from further applications. The main obstacles confronting TMOs are inferior innate conductivity, large volumetric change, and easily particle aggregate during repeated cycling, leading to unsatisfactory cyclability and rate capability [12, 14]. Or, perhaps worse still, drastic volume change will engender serious pulverization problem and even exert bad effect on the safety of a battery [15]. Therefore, substantial attention has been paid to search for feasible approaches to circumvent the aforementioned intractable issues and boost their electrochemical performances.

In general, minishing the size of TMO particles to nanoscale and combining TMOs with carbon nanostructures are judged as two valid strategies to address the issues described above [16–18]. On account of the performance of electroactive materials is closely bound up with the amount of active sites, downsizing TMO particles can increase the active surface area and make it have adequate exposure with the electrolyte, thus leading to high specific capacity and reversibility [19]. In addition, because of the small size effect of nanomaterials, nanoscale TMOs particles have little deformation stress during cycling, which can reduce the structural damage of nanoparticles and warrant an improved cycling stability [20]. Though nanostructured TMOs have adequate surface active sites to get involved in the lithium storage process, the inherent poor conductivity makes it difficult to realize their full potential. In this instance, to further improve its performance, carbon-decorated TMOs nanomaterials emerge as an available tactics. Introducing sp^2-hybridized carbons, such as carbon nanotubes (CNTs) and graphene, to support TMOs nanoparticles can increase the conductivity of TMOs/carbon composites, while also providing buffer space to counteract the stress caused by the repeated lithium insertion/exaction [17]. Beyond that, carbon support with abundant functional groups or heteroatoms could also be conducive to the dispersion of TMOs nanoparticles, which can avoid the agglomeration of active materials. For example, Wang et al. proposed an effective tactic to uniformly anchor tiny SnO_2 nanoparticles on N, S co-doped graphene (NSGS) [21]. Because of having integrated the merits of the aforementioned two methods, such as highly active ultrafine SnO_2 nanoparticles (≈ 5 nm), the coordination effect between well-dispersed SnO_2 and doped graphene, and the improved electrical conductivity, the optimized NSGS composite has superior lithium-storage performance. However, there is a fatal defect in the carbon-decorated approach, that is, the open structure unable to completely avoid the TMOs from migrating, agglomerating, and even detaching from the carbon framework, thus leading to the rapid capacity attenuation [22, 23]. To rationally address the above problem, encapsulating nanostructured TMOs into hollow porous carbon framework has become a meritorious strategy. This method can not only effectively protect the TMOs nanomaterials from aggregating and collapsing, but also provide enough void to alleviate the stress effects caused by volume variations [19]. Consequently, encapsulating nanoscale TMOs in hollow porous carbon-based support has been the priority of tackling the abovementioned intractable issues of TMOs.

Herein, we aim to provide a simple method to construct hierarchical porous metal oxide@carbon (MO@C, MO = MoO_2, V_2O_5, and WO_3) composites for boosting the development of LIBs. Concretely, ultrafine MO nanoparticles were successfully encapsulated and well-distributed in the hierarchical porous carbon framework through a series of process including freeze drying, pyrolysis, and etching. Benefiting from the synergistic effect of nano-scale MO particles and highly conductive carbon skeleton, MO@C composites all manifested exceedingly good electrochemical properties. MoO_2@C composite, for instance, with optimized nanostructure showed supernal initial lithium storage capacity (1513.7 mAh·g^{-1} at 0.1 A·g^{-1}) and rate capability (443.5 mAh·g^{-1} at 5.0 A·g^{-1}). Furthermore, the MoO_2@C anode can still attain a reversible capacity of 901.3 mAh·g^{-1} after 200 cycles at 0.1 A·g^{-1}, and 669.5 mAh·g^{-1} after 1000 cycles at 1.0 A·g^{-1}, indicating outstanding cycling stability.

2 Experimental

2.1 Synthesis of SiO_2 nanospheres

The silica (SiO_2) nanospheres were synthesized by a modified Stöber's method according to the past work [24]. Typically, 10 mL of tetraethyl orthosilicate (TEOS) was ultrasonically dispersed in 90 mL of absolute ethanol to form a homogeneous solution (denoted as solution A). Then, solution B consisting of 10 mL aqueous ammonia, 20 mL distilled (DI) water, and 70 mL absolute ethanol was poured into the above solution A and stirred at 45 °C for 2.5 h. The mixture was gradually changed from transparent solution to white colloidal suspension. Finally, the suspension was centrifuged, washed with DI water and ethanol several times, and the resulting white powder was vacuum-dried at 60 °C for 12 h.

2.2 Synthesis of hierarchical porous MO@C composites

A freeze drying–pyrolysis–etching method was served to synthesize hierarchical porous MO@C composites. Here, we used MoO_2@C composite as an example to illustrate the preparation process elaborately. Typically, 509.7 mg of white silica powders were first ultrasonically dispersed in 60 mL of DI water. Then, 1.085 g of polyvinyl pyrrolidone (PVP) was added into the SiO_2 suspension and ultrasonically treated for another 0.5 h. After the mixture fully dispersed, 20 mL of metal oxyacid salts (also called oxometalates) solution containing 1.833 g ammonium molybdate tetrahydrate ($(NH_4)_6Mo_7O_{24}{\cdot}4H_2O$) was further added into the above mixed solution to get Mo@PVP@SiO_2 precursor solution. Subsequently, the precursor solution was transferred to a heating magnetic whisk, stirred at 85 °C to evaporate some water, and lyophilized in a freeze dryer. After that, the freeze-dried Mo@PVP@SiO_2 precursor was annealed at 700 °C in Ar flow for 2 h to get MoO_2@C@SiO_2 composite. After the sintering process, the black powder was etched at 4 M NH_4HF_2 solution to remove the SiO_2 template. At last, the resulting powder was centrifuged, washed with DI water to neutral, and freeze-dried to get hierarchical porous PVP-derived carbon@MoO_2 (denoted as PCM) composite. Control sample without SiO_2 template was prepared by the freeze drying-pyrolysis procedure, denoted as MoO_2/C composite.

Like the synthesis of hierarchical porous PCM composite, the other hierarchical porous V_2O_5@C and WO_3@C composites can be prepared by the same process except from the different starting metal oxyacid salts (ammonium metavanadate (NH_4VO_3) and ammonium tungstate hydrate ($H_{40}N_{10}O_{41}W_{12}{\cdot}xH_2O$)), named as PCV and PCW, respectively. In addition, V@PVP@SiO_2 precursor was heat-treated at 600 °C for 2 h in air atmosphere instead of 700 °C in Ar atmosphere.

2.3 Materials characterization

The morphologies of hierarchical porous PCM, PCV, and PCW composites were first studied by scanning electron microscopy (SEM, JEOL, Regulus8100). And the porous microstructure details were further characterized by transmission electron microscopy (TEM, JEOL, JEM-F200). An X-ray diffractometer (D/MAX/2500PC, Rigaku) was performed to analyze the composition and crystal structures of the MO@C composites, and Raman spectra of the samples were obtained by a confocal Raman spectrometer (invia Qontor, Renishaw). The valence states of Mo, V, W, O, C, and N elements were evaluated using X-ray

photoelectron spectroscopy (XPS, AXIS SUPRA, Kratos). The contents of MoO_2, V_2O_5, and WO_3 were determined by a thermogravimetric analyzer (TGA, TG209F1, Netzsch), which the temperature ranged from 50 to 700 °C under air atmosphere.

2.4 Electrochemical measurements

All electrochemical measurements were tested in two-electrode CR2032 coin cells which consisted of MO@C electrodes, Li metal foils, and Celgard 2325 polypropylene films. The used electrolyte was a solution of 1 M $LiPF_6$, which dimethyl carbonate/ethylene carbonate (1:1, by volume) were used as the solvent. A slurry-coating method was used for preparing MO@C electrodes. In detail, a slurry consisting of the as-fabricated MO@C composites (80 wt.%), Super P (10 wt.%), and polyvinylidene fluoride (10 wt.%) was coated on a Cu foil, and vacuum-dried at 60 °C overnight to evaporate the N-methyl-2-pyrrolidone (NMP) solvent. After that, the whole Cu foil was cut into pieces of circular discs (12 mm in diameter, average mass loading was 0.7–0.8 mg·cm^{-2}), and then pressed at 10 MPa using a tablet pressing machine. The coin cells were assembled in an Ar-filled glove box. After the activation process of the cells, the electrochemical properties of the cells were carried out on a LAND battery system (CT2001A) and a Gamry (Reference 3000) instrument. Galvanostatic charge/discharge (GCD) and cyclic voltammetry (CV) tests were performed between 0.01 and 3.0 V, and electrochemical impedance spectra (EIS) tests were conducted in the frequency range of 0.01–100 KHz.

3 Results and discussion

Scheme 1 elucidates the construction process of hierarchical porous MO@C composites which is based on a freeze drying–pyrolysis–etching procedure. MO@PVP@SiO_2 precursor solution was first obtained by mixing SiO_2 template, PVP with oxometalates such as ammonium molybdate tetrahydrate ($(NH_4)_6Mo_7O_{24}·4H_2O$) and ammonium metavanadate (NH_4VO_3) in ultrapure water. In this work, a water-evaporation-induced self-assembly mechanism has been proposed to illustrate the formation process of MO@PVP@SiO_2 precursor, which is shown in Fig. S1 in the Electronic Supplementary Material (ESM). At first, SiO_2 nanospheres, PVP molecules, ammonium cations, and oxometalate anions were interacting with each other to form into small PVP-SiO_2-PVP units through electrostatic forces and hydrogen bonds. The abundant of ammonium ions can function as a bridge to connect PVP chains and SiO_2 templates, and the oxometalate anions, such as $Mo_7O_{24}^{6-}$ clusters, have good affinity with organic units, thus contributing to the formation of inorganic/organic hybrid building units. Then, with the evaporation of some water, the PVP-SiO_2-PVP units gradually self-assembled into MO@PVP@SiO_2 supramolecular architecture because of the strong inter-molecular interaction of PVP [25]. Finally, MO@PVP@SiO_2 precursor was obtained after the freeze-drying treatment. After that, the precursor was annealed in a tube furnace or muffle furnace. During the pyrolysis process, metal oxides were formed by *in-situ* decomposition of the oxometalates and meanwhile successfully encapsulated in the PVP-derived carbon framework. The possible decomposition reactions have been shown in the supporting information (Eqs. (S1)–(S3) in the ESM). Finally, the collected MO@C@SiO_2 powders were immersed in NH_4HF_2 solution to remove the SiO_2 template, producing hierarchical porous MO@C composites, which small MO nanoparticles homogeneously covered around the inner surface of carbon shell.

Hard template method is a mature approach to obtaining hollow porous carbon framework with uniform size, which has been widely used for the preparation of carbon-based composites [26]. First, spherical SiO_2 colloids template of around 300 nm in diameter were synthesized by a modified Stöber process (Fig. S2 in the ESM). Typically, due to the abundant silanol groups on its surface, SiO_2 is a popular hard template used for constructing hollow porous nanoarchitectures. On one hand, because the negatively charged surface, many shells such as carbon shells and metal oxide shells, can be formed on the surface of SiO_2. On the other hand, the size and shape of the internal cavities can be controlled just by changing the diameter of SiO_2 template. In addition, oxometalates are a kind of anionic metal oxide clusters which is consisting of early transition metal atoms and bridged oxygen atoms [27]. Owing to the high oxidation states of transition metals, oxometalates can be used as the precursors to obtain various metal oxides. Accordingly, herein, hierarchical porous MO@C composites were prepared by a hard-templating method, in which SiO_2 nanospheres, PVP, and oxometalates were used as template, carbon, and metal source, respectively. The morphology and microstructure of hierarchical porous MoO_2@C (PCM), V_2O_5@C (PCV), and WO_3@C (PCW) composites are shown in Fig. 1 and Fig. S3 in the ESM. The SEM images in Fig.

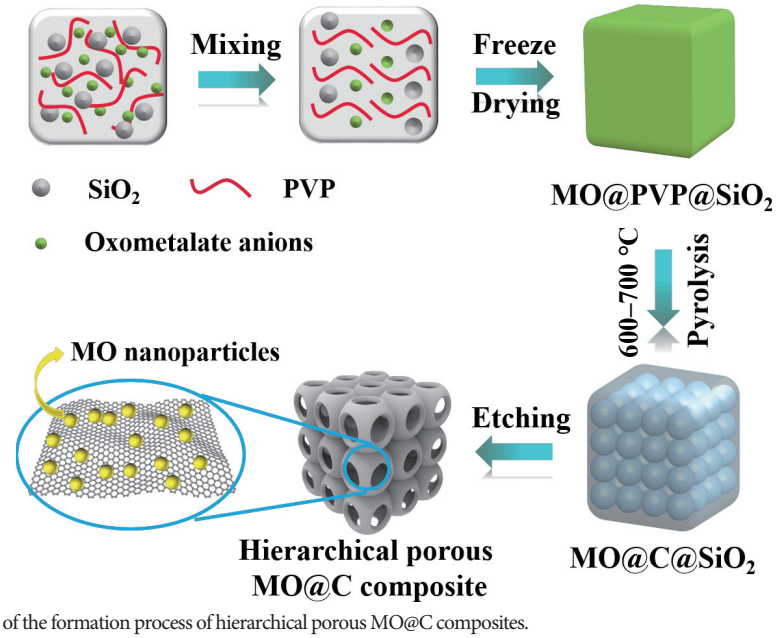

Scheme 1 Schematic illustration of the formation process of hierarchical porous MO@C composites.

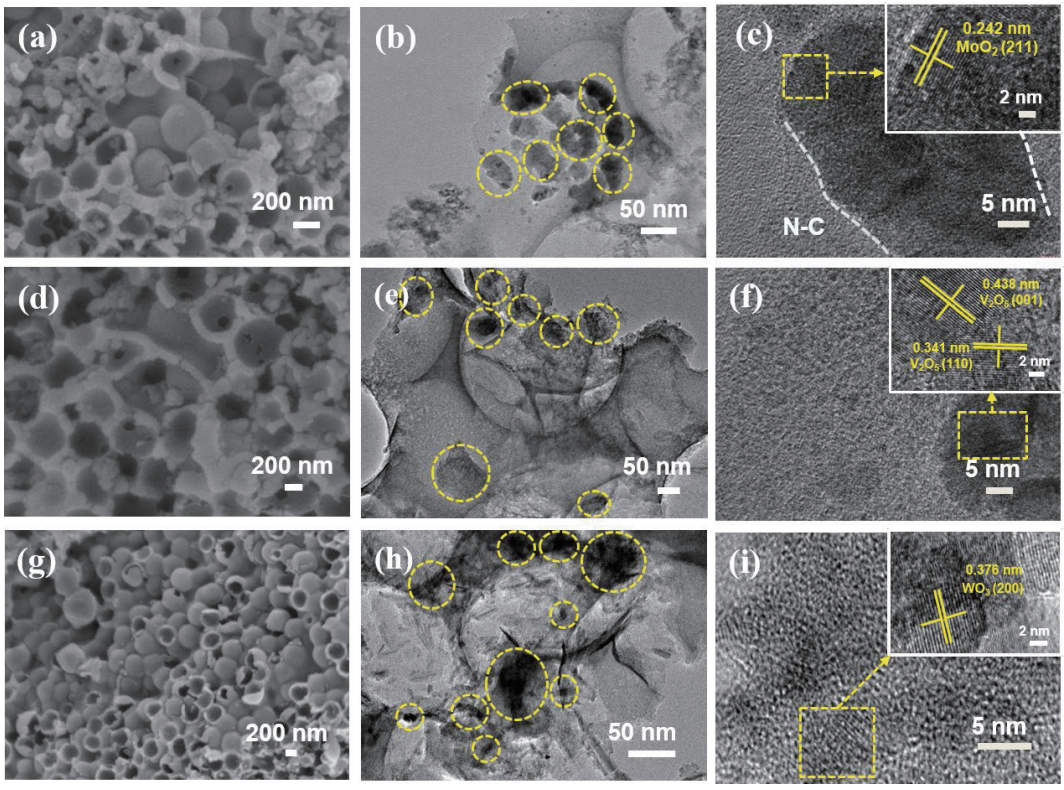

Figure 1 High magnification (a) SEM and (b) TEM images of hierarchical porous PCM composite. (c) HRTEM images of hierarchical porous PCM composite. High magnification (d) SEM and (e) TEM images of hierarchical porous PCV composite. (f) HRTEM images of hierarchical porous PCV composite. High magnification (g) SEM and (h) TEM images of hierarchical porous PCW composite. (i) HRTEM images of hierarchical porous PCW composite. (The areas of yellow circles are the MO nanoparticles.)

S3 in the ESM confirm the successful formation of hierarchical porous structure. High-magnification SEM images in Figs. 1(a), 1(d), and 1(g) further clearly show that small MoO_2, V_2O_5, and WO_3 nanoparticles are well-dispersed and encapsulated in the hierarchical porous carbon framework. The coexistence of mesopores and macropores can function as multi-scale channels for the rapid penetration of electrolyte and lithium-ion (Li^+) transport, which ensures the efficiency of electrochemical reaction [28]. Moreover, the hierarchical porous carbon structure and the voids between MO nanoparticles could provide buffer spaces to accommodate the volume change during the cycling process [20]. And besides, the corresponding Mo, V, and W elements were homogeneously distributed across the respective MoO_2@C, V_2O_5@C, and WO_3@C nanoarchitectures (Fig. S4 in the ESM), indicating that MoO_2, V_2O_5, and WO_3 nanoparticles can be uniformly dispersed in the carbon framework.

TEM investigations were used for further analyzing the microstructure of MO@C composites. As shown in the high magnification TEM images, MoO_2 (Fig. 1(b)), V_2O_5 (Fig. 1(e)), and WO_3 (Fig. 1(h)) nanoparticles (the areas of yellow circles) were evenly encapsulated in the porous carbon framework, which is consisted with the SEM characterizations. High-resolution TEM (HRTEM) images further revealed the successful enclosing of MoO_2 (Fig. 1(c)), V_2O_5 (Fig. 1(f)), and WO_3 (Fig. 1(i)) nanoparticles by the nitrogen-doped carbon (N–C) shell. The PVP-derived N–C shell can not only serve as protection layers to prevent the aggregation and loss of MO nanoparticles, but also function as buffer phase to absorb the stress from volume change, thus endowing the MO@C composites with high specific capacity and favorable cycling stability [29, 30]. Additionally, the N atoms in the carbon shell can produce some morphological defects, further improving the lithium storage performance [16]. The HRTEM image in the inset of Fig. 1(c) reveals a clear lattice fringe spacing of 0.242 nm, corresponding to the (211) plane of monoclinic MoO_2. In the corresponding HRTEM images of PCV (the inset in Fig. 1(f)) and PCW (the inset in Fig. 1(i)) composites, the lattice fringe spacing of 0.438 and 0.341 nm were ascribed to (001) and (110) planes of the orthorhombic V_2O_5, respectively, and the lattice fringe spacing of 0.376 nm was assigned to the (200) facet of cubic WO_3. In addition, hierarchical porous carbon framework (Fig. S5 in the ESM) can be obtained through the same process without the addition of metal sources. As expected, the carbon framework possessed an interconnected 3D porous network with smooth carbon shells, which can warrant the rapid penetration of electrolyte and fast transportation of Li^+ [27].

The crystallographic structures of as-prepared MO@C composites were demonstrated by X-ray diffraction (XRD). As illustrated in Fig. 2(a), the main characteristic peaks of PCM, PCV, and PCW composites are corresponded to monoclinic MoO_2 (JCDPS No. 32-0671), orthorhombic V_2O_5 (JCDPS No. 41-1426), and cubic WO_3 (JCDPS No. 46-1096) respectively, suggesting that oxometalates can be *in-situ* decomposed into its corresponding metal oxides after the annealing treatment. The Raman spectra of PCM, PCV, and PCW composites are presented in Fig. 2(b). For PCM composite, two peaks at about 820.5 and 993.0 cm^{-1} are related to the stretching vibrations of O–Mo–O and Mo=O bonds, and other characteristic peaks at 235.5, 336.0, 469.5, and 663.0 cm^{-1} belong to the vibration modes of MoO_2 [31, 32]. And in the Raman spectra of PCV and PCW composites, typical peaks associated with V_2O_5 (red line) can be clearly confirmed at around 283.5, 406.5, 529.5, 691.5, and 991.5 cm^{-1} [33, 34], while Raman peaks appear at 127.5, 187.5, 247.5, 690.0, and 808.5 cm^{-1} are attributed to the bond vibration modes of cubic WO_3 (blue line) [35]. In addition, two broad peaks centered at around 1360.0 and 1585.5 cm^{-1} correspond to the D and G bands of carbon. The intensity ratio (I_D/I_G) of PCM, PCV, and PCW composites are 1.12, 1.03, and 0.99, respectively, in which PCM composite has the highest I_D/I_G value, suggesting more defects in its carbon skeleton.

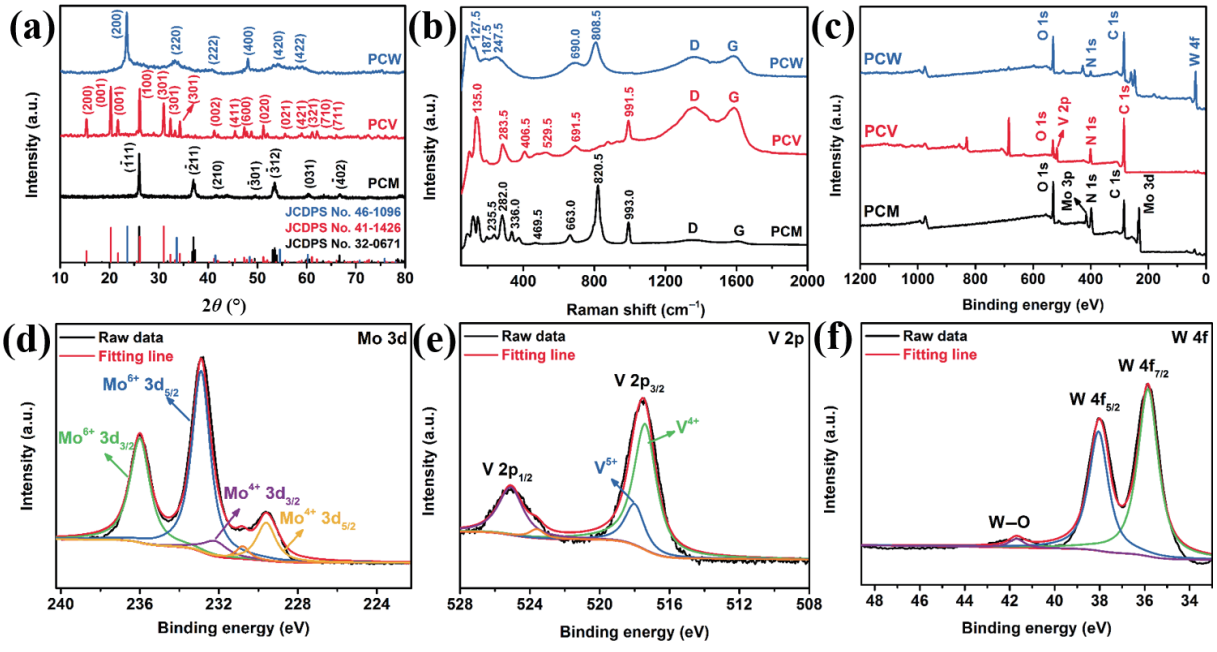

Figure 2 (a) XRD patterns of hierarchical porous MO@C composites. (b) Raman spectra of hierarchical porous MO@C composites. (c) Full-scale XPS spectra of hierarchical porous MO@C composites. High-resolution XPS spectra of (d) Mo 3d, (e) V 2p, and (f) W 4f.

Therefore, the above Raman results indicate a successful conversion from MO@PVP@SiO_2 precursors to MO@C composites after the annealing–etching process.

XPS was employed to further analyze the valance states of the according elements in the MO@C composites. The full XPS survey spectra of PCM, PCV, and PCW composites were shown in Fig. 2(c), in which, the XPS signals of primary elements in the respective composite can be detected. The Mo 3d XPS spectra of PCM composite (Fig. 2(d)) display two pairs of peaks at 232.2/229.6 and 236.0/232.9 eV, corresponding to Mo^{4+} $3d_{3/2}$/Mo^{4+} $3d_{3/2}$ and Mo^{6+} $3d_{3/2}$/Mo^{6+} $3d_{3/2}$, respectively. A pair of Mo^{4+} 3d peaks with a spin energy separation of 2.6 eV can be identified as MoO_2 phase, while the other pair of peaks could be indexed to MoO_3 phase, which is because of the oxidation of MoO_2 in air [12, 36]. For the high-resolution V 2p spectra of PCV composite (Fig. 2(e)), two fitted peaks at 525.1 and 518.0 eV are attributed to V $2p_{1/2}$ and V $2p_{3/2}$ of the V_2O_5 phase, respectively, confirming the presence of tetravalent vanadium [37, 38]. From the W 4f XPS spectra of PCW composite in Fig. 2(f), three peaks at 41.7 (W–O), 38.1(W $4f_{5/2}$), and 35.9 eV (W $4f_{7/2}$) evidence the formation of WO_3 [39]. The high-resolution O 1s spectra of PCM, PCV, and PCW composites are illustrated in Fig. S6(a) in the ESM. The signal peaks at 530.8, 531.6, and 530.9 eV are corresponding to Mo–O, V–O, and W=O bonds, respectively, thus demonstrating the existence of MoO_2, V_2O_5, and WO_3 in the respective composites [12, 37, 38]. In the C 1s spectra (Fig. S6(b) in the ESM), four deconvoluted peaks are present in each MO@C composite, corresponding to C=O, C–O, C–N, and C–C/C=C bonds, respectively. The N 1s spectra in Fig. S6(c) in the ESM reveal that there are three N species in the MO@C composites, namely, graphitic-N, pyrrolic-N, and pyridinic-N. Worth noting that pyridinic-N atoms could act as active sites to enhance the Li-storage capability and graphitic N can improve the conductivity of carbon support, thus leading to higher capability and faster reaction kinetics [40]. The XPS results further confirm the formation of MoO_2, V_2O_5, and WO_3 nanoparticles in the PCM, PCV, and PCW composites. Based on the TGA curves in Fig. S7 in the ESM, the contents of MoO_2, V_2O_5, and WO_3 in the PCM, PCV, and PCW composites were determined to be approximately 80.0 wt.%, 82.2 wt.%, and 78.5 wt.%, respectively.

In order to reveal the uniqueness of our proposed self-assembly mechanism, we replaced ammonium molybdate tetrahydrate with sodium molybdate (Na_2MoO_4) as the molybdenum source. Correspondingly, MoO_2-C composite can be synthesized by the same process. The morphology of MoO_2-C composite is presented in Fig. S8 in the ESM. The SEM images (Figs. S8(a) and S8(b) in the ESM) disclose that the MoO_2-C composite has a cracked bulk structure, in which small MoO_2 nanoparticles are aggregated on the nanoplates. Moreover, the ordered and interconnected porous structure was not formed, indicating that sodium ions can't connect the PVP chains and SiO_2 templates. Corresponding XRD pattern (Fig. S8(c) in the ESM) demonstrates the successful fabrication of MoO_2-C composite. Therefore, we think ammonium ions play an important part in constructing hierarchical porous MO@C composites.

To illustrate just how valuable this simple synthetic strategy is, the as-prepared MO@C composites were evaluated as anode materials in coin-type Li cells. We first used PCM (MoO_2@C) composite as an example to comprehensively illustrate the advantages of MO@C composites as anode material for LIBs. For comparison, porous MoO_2/C composite (Fig. S9 in the ESM) without SiO_2 template was prepared with the similar procedure. The representative CV curves of PCM and MoO_2/C electrodes are presented in Fig. 3(a) and Fig. S10(a) in the ESM. As shown in Fig. 3(a), in the first cathodic cycle, two peaks appeared at about 1.19 and 1.46 V correspond to the formation of Li_xMoO_2 and solid electrolyte interphase (SEI) film [12, 41]. After that, the potential rapidly decreases to 0.01 V, which is due to the alloying reaction of metallic Mo [31]. Two obvious oxidation peaks at around 1.43 and 1.72 V in the first anodic scan are related to the extraction of Li^+. Then the main reduction peaks shift to 1.25 and 1.54 V, while the oxidation peaks have no shift. In addition, the CV curves of PCM electrode is overlapping with each other, revealing an outstanding electrochemical reversibility of MoO_2 during the charging/discharging process [42]. Figure 3(b) and Fig. S10(b) in the ESM manifest the GCD curves of the first four cycles of PCM and MoO_2/C electrodes at 0.1 $A{\cdot}g^{-1}$. In the typical GCD curves of PCM (Fig. 3(b)) and MoO_2/C (Fig. S10(b) in the ESM) electrodes, two gentle slopes can be observed in the discharge/charge curves at about 1.38/1.68 and 1.54/1.27 V, which corresponds with the two pairs of redox peaks in CV curves. This distinctive platform has been detected in other Mo-based composites [43, 44].

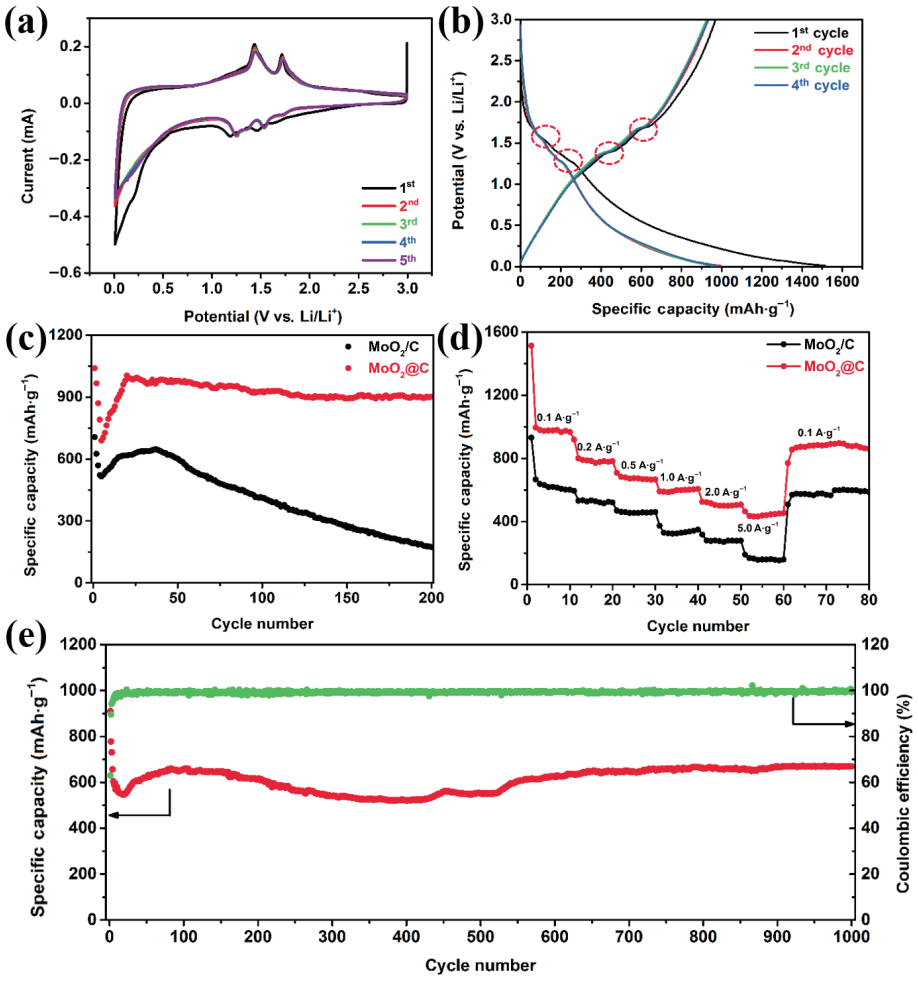

Figure 3 (a) CV curves of the first five cycles of PCM electrode at 0.1 mV·s^{-1}. (b) GCD curves of the first four cycles of hierarchical porous PCM electrode at 0.1 A·g^{-1}. (c) Cycling performance of PCM and MoO_2/C electrodes at 0.1 A·g^{-1}. (d) Rate capability of PCM and MoO_2/C electrodes. (e) Cycling performance of PCM electrode at 1.0 A·g^{-1}.

Similarly, from the second cycle, the GCD curves are almost overlap with each other, indicating a good stability of hierarchical porous MoO_2@C composites. The initial discharge and charge capacity of PCM electrode are 1513.7 and 967.7 mAh·g^{-1} with an initial Coulombic efficiency (CE) of 63.9%, which is slightly lower than that of MoO_2/C (930.7/647.5 mAh·g^{-1}, 69.6%) electrode (Fig. S10(c) in the ESM). The high capacity value of PCM electrode can be competitive with many previously reported Mo-based electrode materials, as shown in Table S1 in the ESM [12, 17, 31, 32, 36, 44–47].

Cycling stability is a significant parameter for the practical application of LIBs. The cycling performance of PCM and MoO_2/C electrodes at 0.1 A·g^{-1} are shown in Fig. 3(c). Obviously, the PCM electrode shows better sustained discharge capacity than that of MoO_2/C electrode. A discharge capacity of 966.0, 688.5, 820.0, 978.5, 927.5, 892.5, and 901.0 mAh·g^{-1} in the 2nd, 5th, 10th, 50th, 100th, 150th, and 200th cycle can be delivered, respectively (Fig. S10(d) in the ESM). Even after 200 cycles, the PCM electrode still delivered a high reversible capacity of 901.0 mAh·g^{-1}, indicating a good stability of the hierarchical porous structure. And noticeably, the final discharge capacity of PCM electrode is higher than the theoretical capacity of MoO_2 (832 mAh·g^{-1}), which can be ascribed to the additional lithium storage sites provided by pyridinic-N atoms [40]. Moreover, due to the intercalation mechanism of carbon materials, hierarchical porous carbon framework also has partly capacity contribution to the overall capacity of PCM electrode (Fig. S11 in the ESM). In addition, at the initial stage of cycling, the capacity of the PCM and MoO_2/C electrodes decrease at first, and then increase. This phenomenon has already been noticed in other TMO-based anode materials [42, 48, 49]. In this circumstance, the fading of capacity in the initial cycles is arising from some irreversible chemical reactions and the formation of unstable SEI layers [42]. Afterwards, stable SEI film is formed and an increasing number of active sites gradually expose to the electrolyte, leading to an increased capacity and improved cyclability [50]. The rate capabilities of PCM and MoO_2/C electrodes were measured from 0.1 to 5.0 A·g^{-1}, and corresponding GCD curves are shown in Figs. S10(e) and S10(f) in the ESM. As presented in Fig. 3(d), the PCM electrode had higher average reversible capacities of 1030.0, 796.0, 675.0, 596.0, 508.0, and 443.5 mAh·g^{-1} at current densities of 0.1, 0.2, 0.5, 1.0, 2.0, and 5.0 A·g^{-1}, respectively. Furthermore, a high capacity of 872.0 mAh·g^{-1} retained as the current density returns to 0.1 A·g^{-1}, suggesting an excellent reversibility of PCM electrode. Long-term cycling property at high current densities is a crucial parameter for the practical application of an anode material. As displayed in Fig. 3(e), the PCM electrode still delivers a high discharge capacity of 669.5 mAh·g^{-1} after 1000 cycles at 1.0 A·g^{-1}. Meanwhile, after 40 cycles, the Coulombic efficiency reaches to about 100.0% and keeps it stable to 1000 cycles. The good cycling stability of the electrode should be attributed to the following two aspects. First, the voids between carbon shells and MoO_2 nanoparticles provide free spaces to accommodate the volume change of MoO_2 nanoparticles. Second, the conductive hierarchical porous carbon framework provides sufficient channels for the penetration of electrolyte and shorten the distance of Li^+ from the active sites [28].

The reaction kinetics of the PCM electrode was examined by

electrochemical impedance spectroscopy (EIS) measurements. The Nyquist plots of PCM and MoO_2/C electrodes are presented in Fig. 4(a). Typical Nyquist diagram includes two regions, the semi-circle region and the long slash region. In general, the Z'-intercept of the curve represents the internal resistance (R_s) of an electrode, while the diameter of the semi-circle expresses the interfacial charge transfer resistance (R_{ct}) [20]. In addition, the slash in the low-frequency region corresponds to Warburg impedance resistance (R_w), which reflects the lithium ion diffusion process [51]. According to the proposed equivalent circuit model in Fig. S12 in the ESM, the R_s and R_{ct} values of the PCM electrode are 0.5 and 503.2 Ω, which is smaller than that of MoO_2/C electrode (Table S2 in the ESM). Based on the empirical formula (Eq. (1)), the lithium ion diffusion coefficient (D_{Li}) is inversely proportional to the square of Warburg factor (σ_w), where σ_w depends on Z' ($Z' \propto \sigma_w^{-1/2}$, Eq. (2)) [52]

$$D_{Li} = R^2T^2/(2A^2n^4F^4C^2\sigma_w^2) \quad (1)$$

$$Z = R_s + R_{ct} + \sigma_w\omega^{-1/2} \quad (2)$$

in the above equations, R, T, and F are the gas constant, absolute temperature, and Faraday constant, respectively, A is the area of the electrode, n is the number of electronic transfer in the electrochemical reaction, C is the concentration of lithium ions, σ_w is the Warburg factor, and ω is the angular frequency. The values of σ_w can be attained from the linear fitting slope of Z'–$\omega^{-1/2}$ plots in the low-frequency region. As can be seen from Fig. 4(b), the PCM electrode has smaller σ_w value than MoO_2/C electrode. Accordingly, it has large D_{Li} value, indicating a great improvement of reaction kinetics. The electrochemical reaction kinetics of the PCM electrode is further examined by CV measurements at different scan rates. As depicted in Fig. 4(c), except for the slight shift of redox peaks, the CV curves of the PCM electrode are nearly identical, indicating a smaller polarization and admirable reaction kinetics of the tested electrode [21]. Generally speaking, the relationship of the scan rates (v) and the currents (i) can be revealed by the following empirical formula: $i = av^b$, where a and b are constant. Usually, the b-value is adjustable from 0.5 to 1.0, where b = 1.0 reveals a capacitive-controlled process and b = 0.5 indicates a diffusion-dominated process [53]. The b-value can be determined by the fitted slope of log(i)–log(v) plots in Fig. 4(d). The b values of the four peaks for PCM electrode are 0.61 (Peak 1), 0.65 (Peak 2), 0.70 (Peak 3), and 0.76 (Peak 4) (Table S3 in the ESM), respectively, revealing that the reaction kinetics is controlled by both processes. In fact, based on the undermentioned formula (Eq. (3)), the overall capacity is the sum of two parts, namely the capacitive contribution (k_1v) plus the diffusion-controlled contribution ($k_2v^{1/2}$) [54, 55]

$$i = k_1v + k_2v^{1/2} \quad (3)$$

As shown in Fig. 4(e), at the scan rate of 0.2 mV·s^{-1}, 59.2% of the storage charge is produced by the capacitive-controlled process, in other words, the capacitive contribution ratio of the PCM electrode accounts for 59.2% of the whole capacity. Similarly, the corresponding capacitive contributions are calculated to be 67.0%, 70.3%, 76.6%, and 82.1% at the scan rate of 0.4, 0.6, 0.8, and 1.0 mV·s^{-1} (Fig. S13 in the ESM), respectively. High capacitive contribution ratios (Fig. 4(f)) are favorable for the transport of ions and electrons, leading to excellent rate performance and cycling stability [20]. In addition, the lithium diffusion behaviors of the PCM and MoO_2/C (Fig. S14(a) in the ESM) electrodes can be further investigated by Randles–Sevcik equation (Eq. (4)) [56]

$$i_p = 0.4463nFAC(nFD_{Li}v/(RT))^{1/2} \quad (4)$$

in this equation, i_p refers to the peak current, the other parameters are consistent with the parameters in Eq.(1). Considering the same fabrication processes of coin-type cells, the above equation (Eq. (4)) can be simplified as: $i_p = kD_{Li}^{1/2}v^{1/2}$ (k is a constant) [57]. Therefore, the D_{Li} could be obtained from the linear fitting slope of i_p–$v^{1/2}$ plots. As clearly seen in Fig. S14(b) in the ESM, all the four peaks of the PCM electrode have higher slope than that of MoO_2/C electrode, meaning that PCM electrode has large D_{Li} value, which consists with the EIS analysis. Hence, the aforementioned analyses corroborate the enhanced reaction kinetics, and meanwhile rationally interpret the reason of the improved lithium storage properties of PCM electrode.

The lithium storage properties of PCV and PCW composites as anode materials are presented in Fig. 5. Figure 5(a) shows the CV curves of the PCV electrode for the first five cycles at 0.1 mV·s^{-1}. In

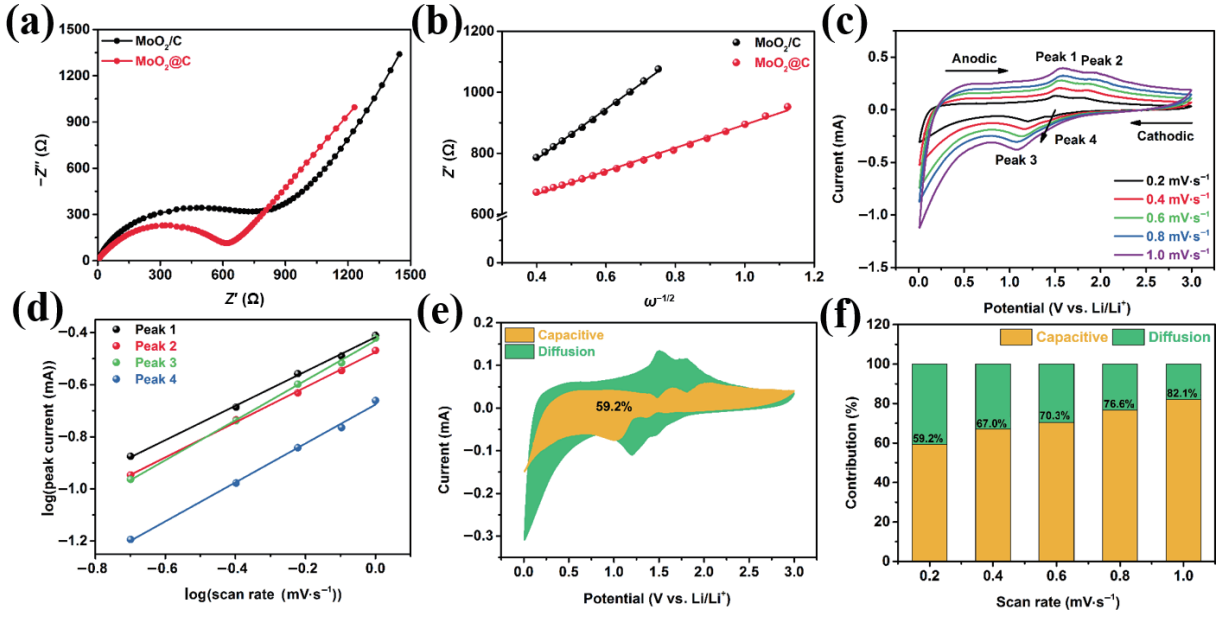

Figure 4 (a) The Nyquist plots of PCM and MoO_2/C electrodes. (b) Z' vs $\omega^{-1/2}$ plot in the low frequency range (the slope of fitting curves is the Warburg factor: σ_w). (c) CV curves of PCM electrode at different scan rates. (d) Relationship between logarithm cathodic peak current and logarithm scan rates of PCM electrode. (e) Capacitive contribution of PCM electrode at 0.2 mV·s^{-1}. (f) Normalized contribution ratio of capacitive and diffusion-controlled capacities of PCM electrode at different scan rates.

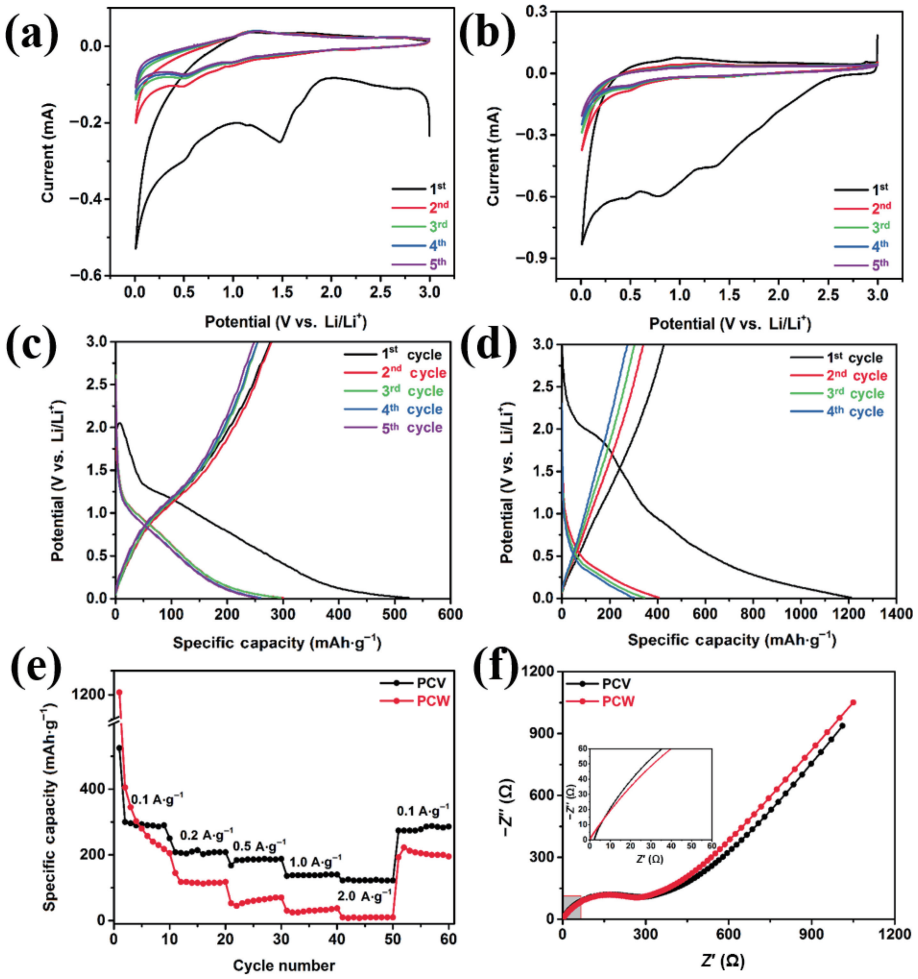

Figure 5 CV curves of the first five cycles of (a) PCV and (b) PCW electrodes at 0.1 mV·s^{-1}. GCD curves of the first five cycles of (c) PCV and (d) PCW electrodes at 0.1 A·g^{-1}. (e) Rate capability of PCV and PCW electrodes. (f) The Nyquist plots of PCV and PCW electrodes at 1.0 A·g^{-1}.

the initial cathodic cycle, an irreversible reduction peak centered at 1.47 V is ascribed to the lithium insertion into V_2O_5 nanoparticles and the formation of SEI films [58, 59]. In the subsequent cycles, two small cathodic peaks at about 0.97 and 0.47 V are related to the reduction reaction of V_2O_5 to metal V, while the anodic peak at around 1.21 V is associated with the oxidation of metal V [60]. Moreover, the CV curves are nearly overlapping with each other from the second cycle, revealing the good reversibility of the electrode. The lithium storage mechanism of WO_3 ($WO_3 + 6Li^+ + 6e^- \leftrightarrow W + 3Li_2O$) is reflected by the redox peaks in the representative CV curves in Fig. 5(b) [61, 62]. And the shapes of the CV curves are identical after the first cycle, illustrating the good reversibility of the PCW electrode. Typical GCD curves (Fig. 5(c)) show that the PCV electrode can deliver an initial discharge/charge capacities of 525.0/278.0 mAh·g^{-1}, respectively, and the initial CE is 53.0%. By contrast, the initial CE of the porous PVP-derived carbon (PC) electrode is only 16.7% (Fig. S11(a) in the ESM), which may be due to the formation of SEI film and excess irreversible absorption of Li^+ within the porous carbon material [63]. However, in Fig. 5(d), the PCW electrode has a high initial discharge capacity of 1210.0 mAh·g^{-1} and a low charge capacity of 425.0 mAh·g^{-1}, corresponding to an ultralow initial CE of 35.1%. The initial capacity loss is a common phenomenon for TMOs-based anode materials, which is mainly resulting from the inevitable formation of SEI films and the occurrence of side reactions [64].

The rate performance of the PCV and PCW electrodes is exhibited in Fig. 5(e). For the PCV electrode, average discharge capacities of 310.9, 207.4, 184.2, 138.4, and 122.6 mAh·g^{-1} can be achieved at respective current densities of 0.1, 0.2, 0.5, 1.0, and 2.0 A·g^{-1}, which is obviously superior to those of the porous PC electrode (Fig. S11(b) in the ESM). And upon the current density returned to 0.1 A·g^{-1}, a reversible capacity of 280.0 mAh·g^{-1} was gradually recovered. While the PCW electrode delivered average discharge capacities of 369.5, 118.5, 60.5, 30.5, and 9.5 mAh·g^{-1} at the current densities of 0.1, 0.2, 0.5, 1.0, and 2.0 A·g^{-1}, respectively, and afterwards a high capacity of 203.5 mAh·g^{-1} can be regained at 0.1 A·g^{-1}. The poor rate performance of PCW electrode needs to be further improved. According to the Nyquist plots in Fig. 5(f), the PCV and PCW electrodes have low values of R_s and R_{ct} (Table S2 in the ESM), indicating that the hierarchical porous N-doped carbon framework can improve the electrical conductivity of the PCV and PCW composites. The long-term cycling stability of the PCV and PCW electrodes are presented in Fig. S15 in the ESM. As shown in Fig. S15 in the ESM, the PCV electrode could deliver a capacity of 128.6 mAh·g^{-1} after 550 cycles at the high-rate current density of 1.0 A·g^{-1}, while the PCW electrode maintained a discharge capacity of 165.0 mAh·g^{-1} after 600 cycles. The above results reveal competitive performance compared to many recently reported V-based and W-based anode materials, as displayed in Tables S4 and S5 in the ESM [39, 65–72]. The electrochemical reaction kinetics of the PCV and PCW electrodes are further examined by CV measurements at different scan rates. Figures S16 and S17 in the ESM show the investigation of the electrochemical reaction kinetics of the PCV and PCW electrodes. As recognized in Figs. S16 (b) and S17 (b) and Table S3 in the ESM, the *b* values of all the peaks in the PCV and PCW electrodes are in the range of 0.5–1.0, indicating that the reaction kinetics is

controlled by the diffusion and capacitive process. In addition, the capacitive-controlled process gradually dominants in the reaction kinetics as the scan rates rise to 1.0 $mV \cdot s^{-1}$ (PCV electrode/64.8%, PCW electrode/62.2%), which is conducive to the ion/electron transport at high current densities [20].

Based on the above results, the superior lithium storage properties of the hierarchical porous MO@C composites can be attributed to the synergetic effect of small metal oxide nanoparticles and hierarchical porous N-doped carbon framework. First, small MO nanoparticles hold inspiring surface chemistry, which warrants sufficient active sites participate in the lithium storage reaction, and meanwhile shortens the lithium diffusion path. Second, the hierarchical porous N-doped carbon framework can reserve more electrolytes and provide multi-scale channels for the rapid penetration of electrolyte. Third, the spaces between MO nanoparticles and the inner voids of hierarchical porous network can accommodate the volume variation of MO nanoparticles, thus avoiding the pulverization and fracturing of active materials. Finally, the N-doped atoms could provide additional active sites for lithium storage. In addition, the N-doped atoms also help the dispersion of small MO nanoparticles.

4 Conclusions

In summary, we have demonstrated a metal oxyacid salts-confined pyrolysis strategy for the fabrication of hierarchical porous MO@C composites. More specially, small MO nanoparticles were successfully confined in the PVP-derived hierarchical porous carbon framework by a three-step process consisting of freeze drying, pyrolysis, and etching processes. Due to the synergetic effect of small metal oxide nanoparticles and hierarchical porous N-doped carbon framework, MO@C composites exhibited good lithium storage properties. Especially, MoO_2@C composite delivered a high initial discharge capacity of 1513.7 $mAh \cdot g^{-1}$ at the current density of 0.1 $A \cdot g^{-1}$. And it also manifested an excellent rate capability with a discharge capacity of 443.5 $mAh \cdot g^{-1}$ at 5.0 $A \cdot g^{-1}$. In addition, the MoO_2@C anode can still achieve a high reversible capacity of 901.3 $mAh \cdot g^{-1}$ after 200 cycles at 0.1 $A \cdot g^{-1}$, and 669.51 $mAh \cdot g^{-1}$ after 1000 cycles at 1.0 $A \cdot g^{-1}$, which demonstrates an excellent cycling stability. This strategy can be extended to fabricate various hierarchical porous metal oxide@carbon composites just by changing the starting template, metal, and carbon sources. And we hope this work could provide a new paradigm for the study of oxometalates as well as polyoxometalates and expand its application.

Acknowledgements

J. J. Lin is supported by the Taishan Scholar Project of Shandong Province (No. tsqn201909115). And this work was partly supported by Qingdao University of Science and Technology Hua Xue 201919 (No. QUSTHX201919).

Electronic Supplementary Material: Supplementary material (schematic illustration of the formation mechanism of MO@PVP@SiO_2 precursor; additional SEM images of SiO_2 nanospheres, PCM, PCV and PCW composites; electron images and corresponding energy dispersive spectroscopy (EDS) element mappings of hierarchical porous PCM, PCV, and PCW composites; SEM and TEM images of hierarchical porous PC and XRD patterns of hierarchical porous PC; High-resolution XPS spectra of hierarchical porous MO@C composites; TGA curves (50–700 °C in air) of hierarchical porous PCM, PCV, and PCW composites; SEM images and XRD patterns of MoO_2-C composite (Na_2MoO_4 as Mo source); SEM images and XRD pattern of porous MoO_2/C composite (without SiO_2 template); CV and GCD curves of PCM and MoO_2/C electrodes; GCD curves and rate capability of hierarchical porous PC electrode; equivalent circuit model of the electrochemical impedance spectra; capacitive contribution of PCM electrode at different scan rates; CV curves of MoO_2/C electrode at different scan rates; cycling performance of PCV and PCW electrodes; CV curves and capacitive contribution of PCV electrode at different scan rates; CV curves and capacitive contribution of PCW electrode at different scan rates; comprehensive performance comparison between our work and other Mo-based anode materials for LIBs; impedance parameters of MoO_2/C, PCM, PCV and PCW electrodes calculated from the equivalent circuit model; comprehensive performance comparison between our work and other V-based anode materials for LIBs; and comprehensive performance comparison between our work and other W-based anode materials for LIBs) is available in the online version of this article at https://doi.org/10.1007/s12274-023-5445-0.

References

[1] Zhang, Y. G.; Zhang, Y. H.; Zhang, H. F.; Bai, L. Q.; Hao, L.; Ma, T. Y.; Huang, H. W. Defect engineering in metal sulfides for energy conversion and storage. *Coord. Chem. Rev.* **2021**, *448*, 214147.

[2] Grey, C. P.; Tarascon, J. M. Sustainability and *in-situ* monitoring in battery development. *Nat. Mater.* **2017**, *16*, 45–56.

[3] Du, R.; Wu, Y. F.; Yang, Y. C.; Zhai, T. T.; Zhou, T.; Shang, Q. Y.; Zhu, L. H.; Shang, C. X.; Guo, Z. X. Porosity engineering of MOF-based materials for electrochemical energy storage. *Adv. Energy Mater.* **2021**, *11*, 2100154.

[4] Zhang, X.; Ju, Z. Y.; Housel, L. M.; Wang, L.; Zhu, Y.; Singh, G.; Sadique, N.; Takeuchi, K. J.; Takeuchi, E. S.; Marschilok, A. C. et al. Promoting transport kinetics in li-Ion battery with aligned porous electrode architectures. *Nano Lett.* **2019**, *19*, 8255–8261.

[5] Zhang, X.; Ju, Z. Y.; Zhu, Y.; Takeuchi, K. J.; Takeuchi, E. S.; Marschilok, A. C.; Yu, G. H. Multiscale understanding and architecture design of high energy/power lithium-ion battery electrodes. *Adv. Energy Mater.* **2020**, *11*, 2000808.

[6] Cong, L. N.; Xie, H. M.; Li, J. H. Hierarchical structures based on two-dimensional nanomaterials for rechargeable lithium batteries. *Adv. Energy Mater.* **2017**, *7*, 1601906.

[7] Sun, D. P.; Tan, Z.; Tian, X. Z.; Ke, F.; Wu, Y. L.; Zhang, J. Graphene: A promising candidate for charge regulation in high-performance lithium-ion batteries. *Nano Res.* **2021**, *14*, 4370–4385.

[8] Yang, C. P.; Fu, K.; Zhang, Y.; Hitz, E.; Hu, L. B. Protected lithium-metal anodes in batteries: From liquid to solid. *Adv. Mater.* **2017**, *29*, 1701169.

[9] Balogun, M. S.; Yu, M. H.; Huang, Y. C.; Li, C.; Fang, P. P.; Liu, Y.; Lu, X. H.; Tong, Y. X. Binder-free Fe_2N nanoparticles on carbon textile with high power density as novel anode for high-performance flexible lithium ion batteries. *Nano Energy* **2015**, *11*, 348–355.

[10] Zhang, G. H.; Hou, S. C.; Zhang, H.; Zeng, W.; Yan, F. L.; Li, C. C.; Duan, H. G. High-performance and ultra-stable lithium-ion batteries based on MOF-derived ZnO@ZnO quantum dots/C core-shell nanorod arrays on a carbon cloth anode. *Adv. Mater.* **2015**, *27*, 2400–2405.

[11] Liu, M.; Fan, H.; Zhuo, O.; Chen, J. C.; Wu, Q.; Yang, L. J.; Peng, L. M.; Wang, X. Z.; Che, R. C.; Hu, Z. A general strategy to construct yolk-shelled metal oxides inside carbon nanocages for high-stable lithium-ion battery anodes. *Nano Energy* **2020**, *68*, 104368.

[12] Zhao, X.; Wang, H. E.; Chen, X. X.; Cao, J.; Zhao, Y. D.; Neale, Z. G.; Cai, W.; Sui, J. H.; Cao, G. Z. Tubular MoO_2 organized by 2D assemblies for fast and durable alkali-ion storage. *Energy Storage Mat.* **2018**, *11*, 161–169.

[13] Zheng, M. B.; Tang, H.; Li, L. L.; Hu, Q.; Zhang, L.; Xue, H. G.; Pang, H. Hierarchically nanostructured transition metal oxides for lithium-ion batteries. *Adv. Sci.* **2018**, *5*, 1700592.

[14] Wang, H. J.; Wang, H.; Zhang, D. X.; Chen, G.; Chen, L.; Zhang,

N.; Ma, R. Z.; Liu, X. H. Double confined MoO_2/Sn/NC@NC nanotubes: Solid-liquid synthesis, conformal transformation, and excellent lithium-ion storage. *ACS Appl. Mater. Interfaces* **2021**, *13*, 19836–19845.

[15] Hou, T. Y.; Liu, B. R.; Sun, X. H.; Fan, A. R.; Xu, Z. K.; Cai, S.; Zheng, C. M.; Yu, G. H.; Tricoli, A. Covalent coupling-stabilized transition-metal sulfide/carbon nanotube composites for lithium/sodium-ion batteries. *ACS Nano* **2021**, *15*, 6735–6746.

[16] Tabassum, H.; Zou, R. Q.; Mahmood, A.; Liang, Z. B.; Wang, Q. F.; Zhang, H.; Gao, S.; Qu, C.; Guo, W. H.; Guo, S. J. A universal strategy for hollow metal oxide nanoparticles encapsulated into B/N co-doped graphitic nanotubes as high-performance lithium-ion battery anodes. *Adv. Mater.* **2018**, *30*, 1705441.

[17] Li, Z.; Wang, C.; Chen, X. Z.; Wang, X. X.; Li, X. Y.; Yamauchi, Y.; Xu, X. J.; Wang, J.; Lin, C. F.; Luo, D. et al. MoO_x nanoparticles anchored on N-doped porous carbon as Li-ion battery electrode. *Chem. Eng. J.* **2020**, *381*, 122588.

[18] Wang, X. F.; Tang, Y. H.; Shi, P. H.; Fan, J. C.; Xu, Q. J.; Min, Y. L. Self-evaporating from inside to outside to construct cobalt oxide nanoparticles-embedded nitrogen-doped porous carbon nanofibers for high-performance lithium ion batteries. *Chem. Eng. J.* **2018**, *334*, 1642–1649.

[19] Huang, Y.; Fang, Y. J.; Lu, X. F.; Luan, D. Y.; Lou, X. W. Co_3O_4 hollow nanoparticles embedded in mesoporous walls of carbon nanoboxes for efficient lithium storage. *Angew. Chem., Int. Ed.* **2020**, *59*, 19914–19918.

[20] Xu, H. Z.; Sun, L.; Li, W.; Gao, M. Y.; Zhou, Q. N.; Li, P.; Yang, S. K.; Lin, J. J. Facile synthesis of hierarchical g-C_3N_4@WS_2 composite as Lithium-ion battery anode. *Chem. Eng. J.* **2022**, *435*, 135129.

[21] Wang, H. G.; Wu, Q.; Wang, Y. H.; Wang, X.; Wu, L. L.; Song, S. Y.; Zhang, H. J. Molecular engineering of monodisperse SnO_2 nanocrystals anchored on doped graphene with high-performance lithium/sodium-storage properties in half/full cells. *Adv. Energy Mater.* **2018**, *9*, 1802993.

[22] Zhang, C. W.; Song, Y.; Xu, L. B.; Yin, F. X. *In-situ* encapsulation of Co/Co_3O_4 nanoparticles in nitrogen-doped hierarchically ordered porous carbon as high performance anode for lithium-ion batteries. *Chem. Eng. J.* **2020**, *380*, 122545.

[23] Pan, L.; Zhang, Y. H.; Lu, F.; Du, Y.; Lu, Z. J.; Yang, Y. J.; Ye, T.; Liang, Q. F.; Bando, Y.; Wang, X. Exposed facet engineering design of graphene-SnO_2 nanorods for ultrastable Li-ion batteries. *Energy Storage Mater.* **2019**, *19*, 39–47.

[24] Azhar, A.; Zakaria, M. B.; Ebeid, E. M.; Chikyow, T.; Bando, Y.; Alshehri, A. A.; Alghamdi, Y. G.; Cai, Z. X.; Kumar, N. A.; Lin, J. J. et al. Synthesis of hollow Co-Fe prussian blue analogue cubes by using silica spheres as a sacrificial template. *ChemistryOpen* **2018**, *7*, 599–603.

[25] Sun, W. H.; Zhou, W. Z. Dual-step reduction of copper and formation mechanism of Cu pseudo-icosahedral microcrystals. *Cryst. Growth Des.* **2022**, *22*, 2611–2619.

[26] Du, J.; Chen, A. B.; Gao, X. Q.; Zhang, Y.; Lv, H. J. Reasonable construction of hollow carbon spheres with an adjustable shell surface for supercapacitors. *ACS Appl. Mater. Interfaces* **2022**, *14*, 11750–11757.

[27] Das, K.; Yan, T. T.; Paul, S.; Qiu, S. L.; Ben, T.; Roy, S. Self-assembly and cascade catalysis by a soft-oxometalate (SOM) system. *Front. Chem.* **2020**, *8*, 601814.

[28] Hou, J. H.; Cao, C. B.; Idrees, F.; Ma, X. L. Hierarchical porous nitrogen-doped carbon nanosheets derived from silk for ultrahigh-capacity battery anodes and supercapacitors. *ACS Nano* **2015**, *9*, 2556–2564.

[29] Wang, J. Y.; Tang, H. J.; Wang, H.; Yu, R. B.; Wang, D. Multi-shelled hollow micro-/nanostructures: Promising platforms for lithium-ion batteries. *Mater. Chem. Front.* **2017**, *1*, 414–430.

[30] Wu, R. B.; Wang, D. P.; Rui, X. H.; Liu, B.; Zhou, K.; Law, A. W. K.; Yan, Q. Y.; Wei, J.; Chen, Z. *In-situ* formation of hollow hybrids composed of cobalt sulfides embedded within porous carbon polyhedra/carbon nanotubes for high-performance lithium-ion batteries. *Adv. Mater.* **2015**, *27*, 3038–3044.

[31] Wang, C. L.; Sun, L. S.; Zhang, F. F.; Wang, X. X.; Sun, Q. J.; Cheng, Y.; Wang, L. M. Formation of Mo-polydopamine hollow spheres and their conversions to MoO_2/C and Mo_2C/C for efficient electrochemical energy storage and catalyst. *Small* **2017**, *13*, 1701246.

[32] Ni, J. F.; Zhao, Y.; Li, L.; Mai, L. Q. Ultrathin MoO_2 nanosheets for superior lithium storage. *Nano Energy* **2015**, *11*, 129–135.

[33] Jampani, P. H.; Velikokhatnyi, O.; Kadakia, K.; Hong, D. H.; Damle, S. S.; Poston, J. A.; Manivannan, A.; Kumta, P. N. High energy density titanium doped-vanadium oxide-vertically aligned CNT composite electrodes for supercapacitor applications. *J. Mater. Chem. A* **2015**, *3*, 8413–8432.

[34] Chen, Y. P.; Yang, G.; Zhang, Z. H.; Yang, X. Y.; Hou, W. H.; Zhu, J. J. Polyaniline-intercalated layered vanadium oxide nanocomposites-one-pot hydrothermal synthesis and application in lithium battery. *Nanoscale* **2010**, *2*, 2131–2138.

[35] Xiao, Y.; Jiang, M. X.; Cao, M. H. Developing WO_3 as high-performance anode material for lithium-ion batteries. *Mater. Lett.* **2021**, *285*, 129129.

[36] Sun, Y. M.; Hu, X. H.; Luo, W.; Huang, Y. H. Self-assembled hierarchical MoO_2/graphene nanoarchitectures and their application as a high-performance anode material for lithium-ion batteries. *ACS Nano* **2011**, *5*, 7100–7107.

[37] Zhang, Y. Z.; Ge, X.; Kang, Q.; Kong, Z. K.; Wang, Y. L.; Zhan, L. Vanadium oxide nanorods embed in porous graphene aerogel as high-efficiency polysulfide-trapping-conversion mediator for high performance lithium-sulfur batteries. *Chem. Eng. J.* **2020**, *393*, 124570.

[38] Wang, Y.; Jiao, Y. Q.; Yan, H. J.; Yang, G. C.; Tian, C. G.; Wu, A. P.; Liu, Y.; Fu, H. G. Vanadium-incorporated CoP_2 with lattice expansion for highly efficient acidic overall water splitting. *Angew. Chem., Int. Ed.* **2022**, *61*, e202116233.

[39] Yoon, S.; Woo, S. G.; Jung, K. N.; Song, H. Conductive surface modification of cauliflower-like WO_3 and its electrochemical properties for lithium-ion batteries. *J. Alloys Compd.* **2014**, *613*, 187–192.

[40] Shi, R. Y.; Han, C. P.; Xu, X. F.; Qin, X. Y.; Xu, L.; Li, H. F.; Li, J. Q.; Wong, C. P.; Li, B. H. Electrospun N-doped hierarchical porous carbon nanofiber with improved degree of graphitization for high-performance lithium ion capacitor. *Chem. —Eur. J.* **2018**, *24*, 10460–10467.

[41] Chen, N.; Yao, Y.; Wang, D. X.; Wei, Y. J.; Bie, X. F.; Wang, C. Z.; Chen, G.; Du, F. $LiFe(MoO_4)_2$ as a novel anode material for lithium-Ion batteries. *ACS Appl. Mater. Interfaces* **2014**, *6*, 10661–10666.

[42] Zhu, J. K.; Tu, W. M.; Pan, H. F.; Zhang, H.; Liu, B.; Cheng, Y. P.; Deng, Z.; Zhang, H. N. Self-templating synthesis of hollow Co_3O_4 nanoparticles embedded in N, S-dual-doped reduced graphene oxide for lithium ion batteries. *ACS Nano* **2020**, *14*, 5780–5787.

[43] Shen, Y. H.; Jiang, Y. L.; Yang, Z. Z.; Dong, J.; Yang, W.; An, Q. Y.; Mai, L. Q. Electronic structure modulation in MoO_2/MoP heterostructure to induce fast electronic/ionic diffusion kinetics for lithium storage. *Adv. Sci.* **2022**, *9*, 2104504.

[44] Zhang, H. J.; Wang, K. X.; Wu, X. Y.; Jiang, Y. M.; Zhai, Y. B.; Wang, C.; Wei, X.; Chen, J. S. MoO_2/Mo_2C heteronanotubes function as high-performance Li-Ion battery electrode. *Adv. Funct. Mater.* **2014**, *24*, 3399–3404.

[45] Guo, B. K.; Fang, X. P.; Li, B.; Shi, Y. F.; Ouyang, C. Y.; Hu, Y. S.; Wang, Z. X.; Stucky, G. D.; Chen, L. Q. Synthesis and lithium storage mechanism of ultrafine MoO_2 nanorods. *Chem. Mater.* **2012**, *24*, 457–463.

[46] Ihsana, M.; Wang, H. Q.; Majid, S. R.; Yang, J. P.; Kennedy, S. J.; Guo, Z. P.; Liu, H. K. MoO_2/Mo_2C/C spheres as anode materials for lithium ion batteries. *Carbon* **2016**, *96*, 1200–1207.

[47] Yang, X.; Li, Q.; Wang, H. J.; Feng, J.; Zhang, M.; Yuan, R.; Chai, Y. Q. *In-situ* carbonization for template-free synthesis of MoO_2-Mo_2C-C microspheres as high-performance lithium battery anode. *Chem. Eng. J.* **2018**, *337*, 74–81.

[48] Um, J. H.; Palanisamy, K.; Jeong, M.; Kim, H.; Yoon, W. S. Phase dynamics on conversion-reaction-based Tin-doped ferrite anode for next-generation lithium batteries. *ACS Nano* **2019**, *13*, 5674–5685.

[49] Huang, Y.; Xu, Z. H.; Mai, J. Q.; Lau, T. K.; Lu, X. H.; Hsu, Y. J.; Chen, Y. S.; Lee, A. C.; Hou, Y. L.; Meng, Y. S. et al. Revisiting the origin of cycling enhanced capacity of Fe_3O_4 based nanostructured electrode for lithium ion batteries. *Nano Energy* **2017**, *41*, 426–433.

[50] Liu, Y.; Chen, Z. L.; Jia, H. X.; Xu, H. B.; Liu, M.; Wu, R. B. Iron-doping-induced phase transformation in dual-carbon-confined cobalt diselenide enabling superior lithium storage. *ACS Nano* **2019**, *13*, 6113–6124.

[51] Yu, B.; Huang, A. J.; Chen, D. J.; Srinivas, K.; Zhang, X. J.; Wang, X. Q.; Wang, B.; Ma, F.; Liu, C. L.; Zhang, W. L. et al. *In-situ* construction of Mo_2C quantum dots-decorated CNT networks as a multifunctional electrocatalyst for advanced lithium-sulfur batteries. *Small* **2021**, *17*, 2100460.

[52] Shi, N. X.; Xi, B. J.; Huang, M.; Ma, X. J.; Li, H. B.; Feng, J. K.; Xiong, S. L. Hierarchical octahedra constructed by Cu_2S/MoS_2⊂carbon framework with enhanced sodium storage. *Small* **2020**, *16*, 2000952.

[53] Zhu, Y. R.; Li, J. Y.; Yun, X. R.; Zhao, G. G.; Ge, P.; Zou, G. Q.; Liu, Y.; Hou, H. S.; Ji, X. B. Graphitic carbon quantum dots modified nickel cobalt sulfide as cathode materials for alkaline aqueous batteries. *Nano-Micro Lett.* **2020**, *12*, 16.

[54] Li, B. S.; Xi, B. J.; Feng, Z. Y.; Lin, Y.; Liu, J. C.; Feng, J. K.; Qian, Y. T.; Xiong, S. L. Hierarchical porous nanosheets constructed by graphene-coated, interconnected TiO_2 nanoparticles for ultrafast sodium storage. *Adv. Mater.* **2018**, *30*, 1705788.

[55] He, Z. S.; Huang, L. A.; Guo, J. F.; Pei, S. E.; Shao, H. B.; Wang, J. M. Novel hierarchically branched CoC_2O_4@CoO/Co composite arrays with superior lithium storage performance. *Energy Storage Mater.* **2020**, *24*, 362–372.

[56] Qin, J.; Wang, T. S.; Liu, D. Y.; Liu, E. Z.; Zhao, N. Q.; Shi, C. S.; He, F.; Ma, L. Y.; He, C. N. A top-down strategy toward SnSb in-plane nanoconfined 3D N-doped porous graphene composite microspheres for high performance Na-ion battery anode. *Adv. Mater.* **2018**, *30*, 1704670.

[57] Cuan, J.; Zhang, F.; Zheng, Y.; Zhou, T. F.; Liang, G. M.; Guo, Z. P.; Pang, W. K.; Yu, X. B. Heterocarbides reinforced electrochemical energy storage. *Small* **2019**, *35*, 1903652.

[58] Wang, X. C.; Huang, Y. D.; Jia, D. Z.; Pang, W. K.; Guo, Z. P.; Du, Y. P.; Tang, X. C.; Cao, Y. L. Self-assembled sandwich-like vanadium oxide/graphene mesoporous composite as high-capacity anode material for lithium ion batteries. *Inorg. Chem.* **2015**, *54*, 11799–11806.

[59] Li, Y. T.; Zhang, S.; Wang, S. T.; Leng, J.; Jiang, C. H.; Ren, X. W.; Zhang, Z. T.; Yang, Y.; Tang, Z. L. A multi-shelled V_2O_3/C composite with an overall coupled carbon scaffold enabling ultrafast and stable lithium/sodium storage. *J. Mater. Chem. A* **2019**, *7*, 19234–19240.

[60] Fernando, J. F. S.; Siriwardena, D. P.; Firestein, K. L.; Zhang, C.; von Treifeldt, J. E.; Lewis, C. E. M.; Wang, T.; Dubal, D. P.; Golberg, D. V. Enriched pseudocapacitive lithium storage in electrochemically activated carbonaceous vanadium(IV, V) oxide hydrate. *J. Mater. Chem. A* **2020**, *8*, 13183–13196.

[61] Xiong, D. B.; Li, X. F.; Bai, Z. M.; Shan, H.; Fan, L. L.; Wu, C. X.; Li, D. J.; Lu, S. G. Superior cathode performance of nitrogen-doped graphene frameworks for lithium ion batteries. *ACS Appl. Mater. Interfaces* **2017**, *9*, 10643–10651.

[62] Bekarevich, R.; Pihosh, Y.; Tanaka, Y.; Nishikawa, K.; Matsushita, Y.; Hiroto, T.; Ohata, H.; Ohno, T.; Minegishi, T.; Sugiyama, M. et al. Conversion reaction in the binder-free anode for fast-charging Li-ion batteries based on WO_3 nanorods. *ACS Appl. Energy Mater.* **2020**, *3*, 6700–6708.

[63] Li, X.; Sun, X. H.; Hu, X. D.; Fan, F. R.; Cai, S.; Zheng, C. M.; Stucky, G. D. Review on comprehending and enhancing the initial Coulombic efficiency of anode materials in lithium-ion/sodium-ion batteries. *Nano Energy* **2020**, *77*, 105143.

[64] Wang, C. Y.; Zhao, Y. J.; Zhou, L. L.; Liu, Y.; Zhang, W.; Zhao, Z. W.; Hozzein, W. N.; Alharbi, H. M. S.; Li, W.; Zhao, D. Y. Mesoporous carbon matrix confinement synthesis of ultrasmall WO_3 nanocrystals for lithium ion batteries. *J. Mater. Chem. A* **2018**, *6*, 21550–21557.

[65] Wang, H. E.; Zhao, X.; Yin, K. L.; Li, Y.; Chen, L. H.; Yang, X. Y.; Zhang, W. J.; Su, B. L.; Cao, G. Z. Superior pseudocapacitive lithium-ion storage in porous vanadium oxides@C heterostructure composite. *ACS Appl. Mater. Interfaces* **2017**, *9*, 43665–43673.

[66] Li, L. Y.; Liu, P. C.; Zhu, K. J.; Wang, J.; Liu, J. S.; Qiu, J. H. A general and simple method to synthesize well-crystallized nanostructured vanadium oxides for high performance Li-ion batteries. *J. Mater. Chem. A* **2015**, *3*, 9385–9389.

[67] Glushenkov, A. M.; Hassan, M. F.; Stukachev, V. I.; Guo, Z. P.; Liu, H. K.; Kuvshinov, G. G.; Chen, Y. Growth of V_2O_5 nanorods from ball-milled powders and their performance in cathodes and anodes of lithium-ion batteries. *J. Solid State Electrochem.* **2010**, *14*, 1841–1846.

[68] Liu, P. C.; Zhu, K. J.; Xu, Y.; Bian, K.; Wang, J.; Tai, G. A.; Gao, Y. F.; Luo, H. J.; Liu, J. S. Hierarchical porous intercalation-type V_2O_3 as high-performance anode materials for Li-ion batteries. *Chem. —Eur. J.* **2017**, *23*, 7538–7544.

[69] Li, X. X.; Fu, J. J.; Pan, Z. G.; Su, J. J.; Xu, J. W.; Gao, B.; Peng, X.; Wang, L.; Zhang, X. M.; Chu, P. K. Peapod-like V_2O_3 nanorods encapsulated into carbon as binder-free and flexible electrodes in lithium-ion batteries. *J. Power Sources* **2016**, *331*, 58–66.

[70] Li, P.; Li, X.; Zhao, Z. Y.; Wang, M. S.; Fox, T.; Zhang, Q.; Zhou, Y. Correlations among structure, composition and electrochemical performances of WO_3 anode materials for lithium ion batteries. *Electrochim. Acta* **2016**, *192*, 148–157.

[71] Gu, Z. J.; Li, H. Q.; Zhai, T. Y.; Yang, W. S.; Xia, Y. Y.; Ma, Y.; Yao, J. N. Large-scale synthesis of single-crystal hexagonal tungsten trioxide nanowires and electrochemical lithium intercalation into the nanocrystals. *J. Solid State Chem.* **2007**, *180*, 98–105.

[72] Duan, X. C.; Xiao, S. H.; Wang, L. L.; Huang, H.; Liu, Y.; Li, Q. H.; Wang, T. H. Ionic liquid-modulated preparation of hexagonal tungsten trioxide mesocrystals for lithium-ion batteries. *Nanoscale* **2015**, *7*, 2230–2234.